NANO LETTERS

pubs.acs.org/NanoLett Letter

Bringing Electrochemical Three-Dimensional Printing to the Nanoscale

Julian Hengsteler, Barnik Mandal, Cathelijn van Nisselroy, Genevieve P. S. Lau, Tilman Schlotter, Tomaso Zambelli, and Dmitry Momotenko*

Cite This: *Nano Lett.* 2021, 21, 9093−9101 Read Online

ACCESS | Metrics & More | Article Recommendations | Supporting Information

Downloaded via 85.3.213.2 on March 6, 2024 at 09:56:32 (UTC).
See https://pubs.acs.org/sharingguidelines for options on how to legitimately share published articles.

ABSTRACT: Nanoscale 3D printing is attracting attention as an alternative manufacturing technique for a variety of applications from electronics and nanooptics to sensing, nanorobotics, and energy storage. The constantly shrinking critical dimension in state-of-the-art technologies requires fabrication of complex conductive structures with nanometer resolution. Electrochemical techniques are capable of producing impurity-free metallic conductors with superb electrical and mechanical properties, however, true nanoscale resolution (<100 nm) remained unattainable. Here, we set new a benchmark in electrochemical 3D printing. By employing nozzles with dimensions as small as 1 nm, we demonstrate layer-by-layer manufacturing of 25 nm diameter voxels. Full control of the printing process allows adjustment of the feature size on-the-fly, printing tilted, and overhanging structures. On the basis of experimental evidence, we estimate the limits of electrochemical 3D printing and discuss the origins of this new resolution frontier.

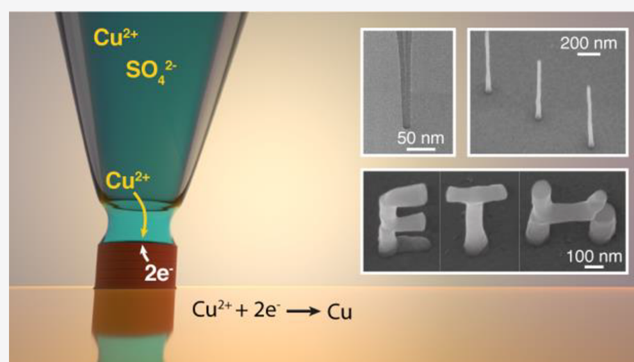

KEYWORDS: *meniscus-confined, electrodeposition, additive manufacturing, nanopipette, metal printing*

Fabrication of complex arbitrary-shaped objects with nanoscale dimensions determines the future development in a variety of disciplines. Advanced optical technologies,[1] sensing,[2] micro- and nanorobotics,[3−5] and more efficient energy storage,[6−8] all require structural and functional elements with feature sizes in the nanometer scale. While conventional planar fabrication technologies are often incapable to produce intricate 3D designs, additive manufacturing (AM), or 3D printing, offers an enormous potential for direct production of complex architectures.

Among existing nanoscale 3D printing techniques, stereolithography is probably the most advanced in producing complex objects composed of voxels with dimensions down to 65 nm.[9,10] However, optical methods typically process only a limited class of materials, such as photoresists, which exhibit rather narrow mechanical, optical, and electrical characteristics. Electrically conductive features, much needed for many applications, have been produced with another family of methods, such as focused electron or ion beam techniques,[11−13] which offer probably the highest AM resolution down to 8 nm.[14] Their major drawback is the high carbon contamination due to the organic components in the precursor gas[15] that often makes the as-printed features unsuitable for applications, especially in fields like nanoelectronics or nanooptics, thus rendering the need for postprocessing.

In this light, electrochemical AM is advantageous, as it enables the production of dense conductive materials directly in a single step.[16] Electrochemistry offers intrinsic simplicity, high degree of control over the morphology of the resulting features,[17] and simpler impurity or composition content management.[18] For microscale electrochemical 3D printing, the deposition has to be confined to a small area by localized delivery of a precursor species in a liquid bath.[19,20] Although this allowed fabrication of impressively complex features, like a 1:70 000 replica of a Michelangelo's David,[21] it seems difficult to achieve higher confinement below the submicroscale in liquid environment.[22] A strategy to overcome this issue is to confine the electroplating process within a liquid meniscus formed in air between a capillary tip and a substrate.[17,23−25] A way to achieve smaller feature dimensions is to employ print nozzles with smaller openings. This rather trivial idea is, however, difficult to implement in practice, as it requires high precision in synchronizing nozzle movement with feature growth with increasing probability of tip clogging or losing the

Received: July 22, 2021
Revised: October 12, 2021
Published: October 26, 2021

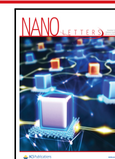

ACS Publications
© 2021 The Authors. Published by American Chemical Society

https://doi.org/10.1021/acs.nanolett.1c02847
Nano Lett. 2021, 21, 9093−9101

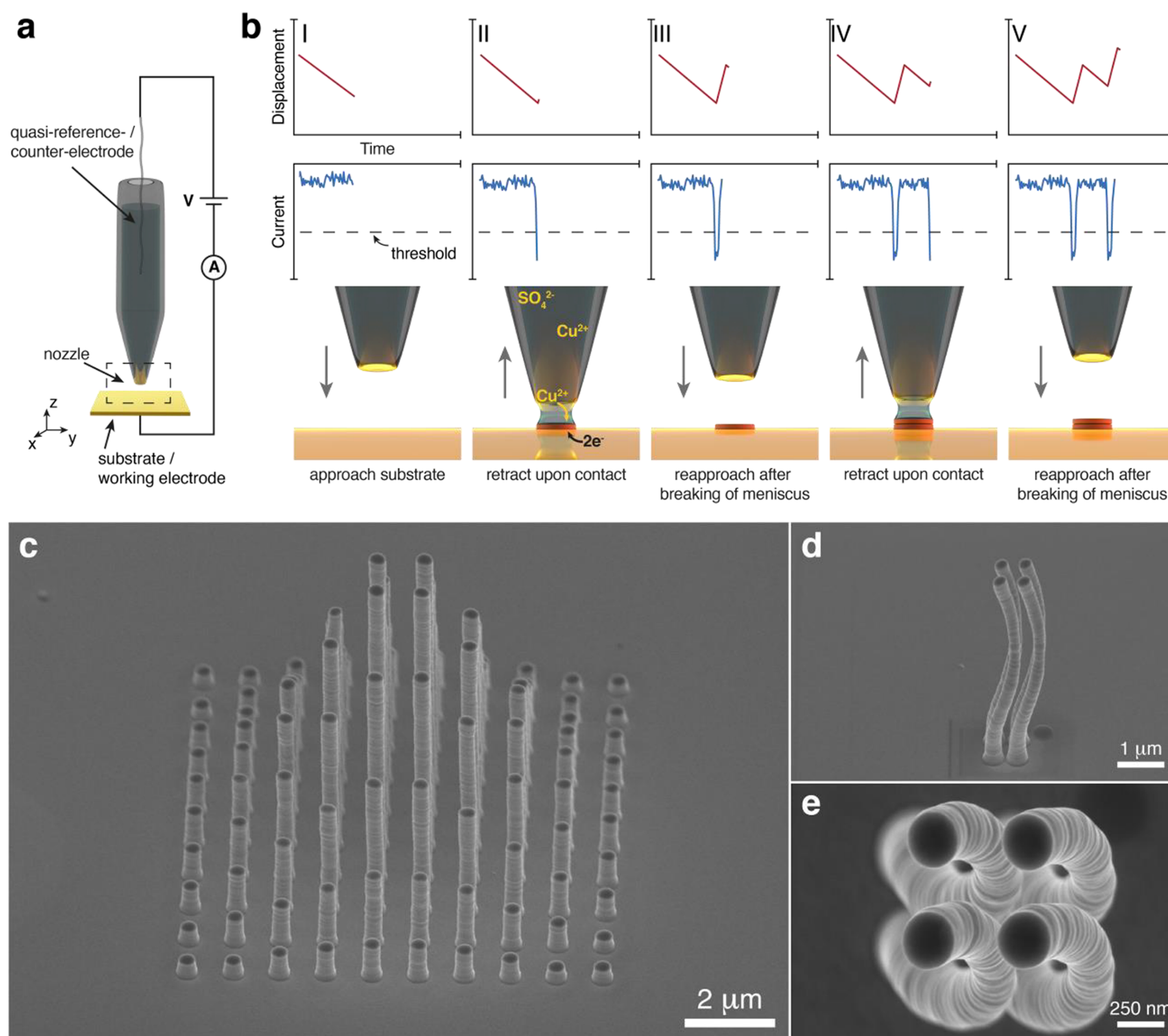

Figure 1. (a) Schematic of the printing setup. The nozzle, containing the electrolyte solution and the quasi-reference counter electrode, is placed above a conductive substrate that constitutes the working electrode of the two-electrode electrochemical cell. The substrate and the nozzle are translated with respect to each other by piezoelectric nanopositioners. (b) Schematic of the printing process of a voxel. A negative voltage is applied between the substrate and the quasi-reference/counter-electrode. (I,II) The pipette approaches the substrate until the current drops below a preset threshold value due to the formation of a liquid meniscus. The copper cations in the electrolyte are reduced to copper on the substrate. (III) To prevent copper growth into the nozzle, the pipette is retracted immediately after the faradaic current reaches the threshold until the meniscus is broken and hence electrodeposition is halted. (IV,V) This procedure is repeated until a certain voxel height is reached. The gray arrows next to the nozzle indicate the direction of the vertical movement of the nozzle. The current and distance graphs in the top row depict the vertical piezo displacement (upper, red) and the evolution of the electrical current (lower, blue) during the printing process. (c−e) Electron microscope images of 3D printed structures with a 253 nm nozzle. (c) Sideview of a 10 × 10 array of pillars (656 voxels) forming a Gaussian peak with increasing heights toward the center of the array. Side (d) and top (e) view on four helical structures printed with a center-to center spacing of 500 nm.

meniscus. Previous attempts to print with nanoscale nozzles failed to bring the resolution below the 100 nm mark and the best to date resolution in printing copper structures (highly conductive and commonly used in nanoelectronics) is 250 nm.[26]

Herein, we introduce a novel approach for electrochemical AM capable of producing 3D nanoscale features in a fully automated manner. Our printing strategy, based on rapid forming and breaking of the meniscus, allows precise control of the printing process with the possibility to tune the voxel size on-the-fly and is perfectly fitted for nanofabrication in a layer-by-layer manner. Using ultrasmall nozzles with diameters as small as 1.6 nm, we approach the resolution frontier of electrochemical 3D printing with feature sizes around 25 nm.

Printing Principle. Figure 1a illustrates the experimental setup for meniscus-confined electrochemical AM. It consists of a print nozzle filled with electrolyte solution containing metal precursor ions (herein, Cu^{2+}), and a conductive substrate, which is biased with respect to a quasi-reference counter electrode inside the capillary. Precise positioning of the nozzle is achieved with an integrated micro- and nanopositioning system that combines micromotors for coarse movement and fine nanoscale translation with piezo actuators.

Herein, we employed quartz nanopipettes with opening diameters of 1.6 ± 0.7, 2 ± 1, 45 ± 10 and 253 ± 88 nm (Supporting Information SI-1) as print nozzles. As the probability of aperture clogging by the electrodeposited feature increases at the nanoscale, we introduced an automated

https://doi.org/10.1021/acs.nanolett.1c02847
Nano Lett. 2021, 21, 9093−9101

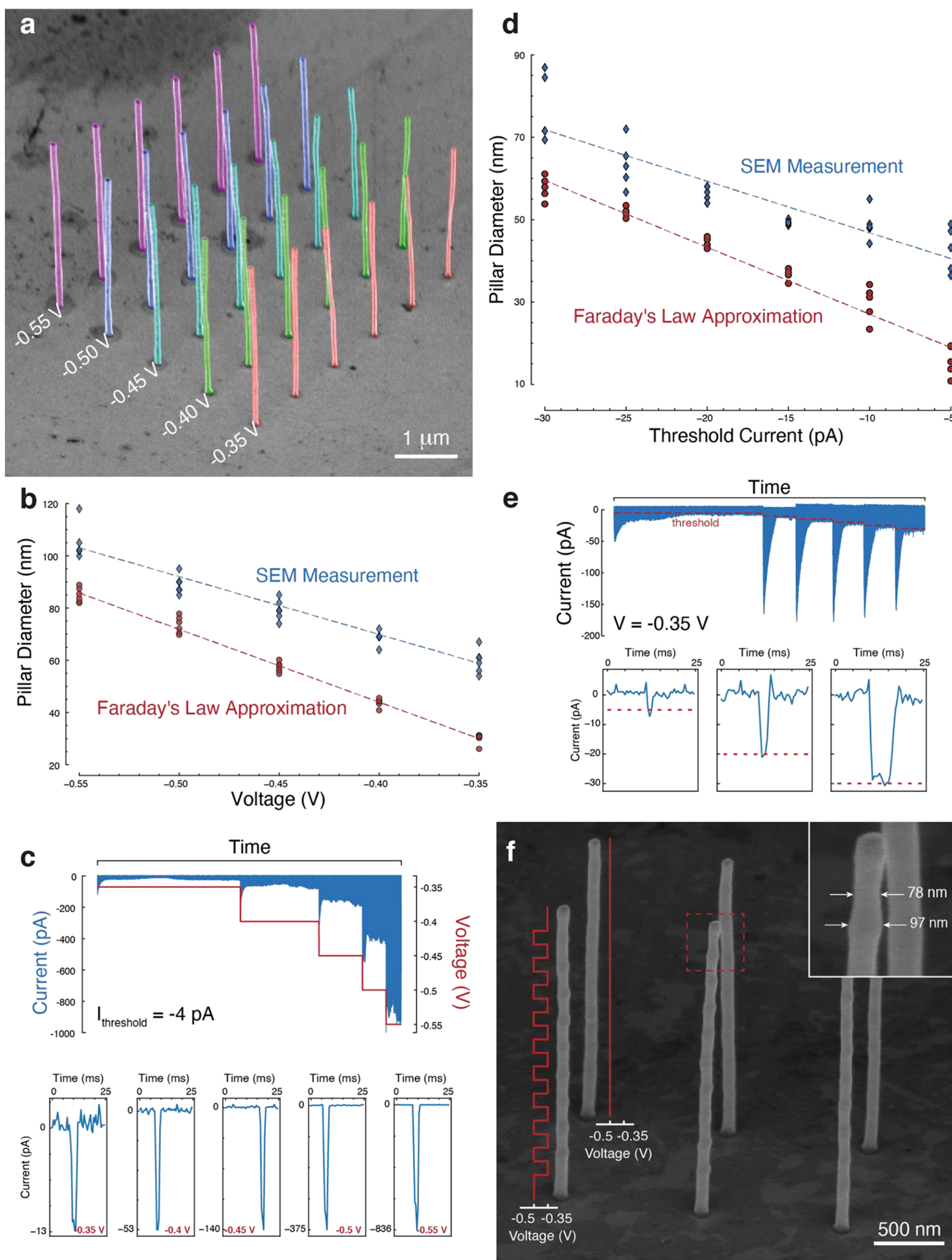

Figure 2. Voltage and set point control of the printing process. (a) False color SEM image of a 5 by 6 array of pillars with a height of 3 μm. The overlaid text indicates the voltage at which the pillars of the respective line were printed. (b) Printed pillar diameters as a function of printing voltage as measured (from SEM image in (a), blue diamonds) and calculated (red circles) from Faraday's law of electrolysis. The dotted lines show the linear trend relating pillar diameter and printing voltage. (c) Current traces for the voltage test (top) and individual peaks at different voltages. (d) Printed pillar diameters as the function of threshold current. (e) Current trace of pillars printed at different threshold set points (top) with close ups of individual current peaks at thresholds of −5, −20, and −30 pA, as indicated by the red dotted lines. (f) SEM image of pillars with (front row) and without (rear row) diameter modulation printed with a pipette with an opening size of about 50 nm. All pillars were printed layer by layer with voxel heights of 100 nm. For the front row the voltages were alternated between −0.5 and −0.35 V, as illustrated with the red solid lines along two pillars. The rear row was consistently printed with −0.5 V. By changing the voltage the voxel diameter is changed by 19 nm ranging from 78 nm (±1.7 nm, −0.35 V) to 97 nm (±1.7 nm, −0.5 V).

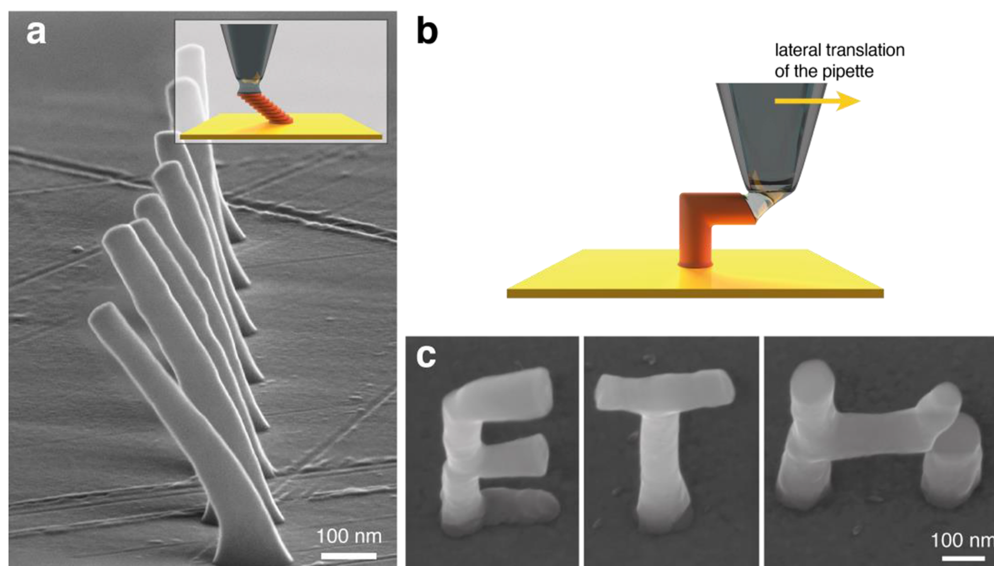

Figure 3. Printed tilted and overhanging features all printed with a 45 nm nozzle opening. (a) SEM images of tilted pillars, printed by stacking voxels with a lateral shift as illustrated in the inset. All pillars were printed with voxel heights of 10 nm. The lateral shift was increased by 2 nm from pillar to pillar, starting in the back with 0 nm up to a 14 nm lateral shift per voxel for the front most pillar. Each pillar has a vertical base voxel of 145 nm height. The SEM image shown is a combination of 5 SEM images shot at an 80° tilt angle overlaid to show all pillars in focus. (b) A schematic showing printing strategy employed to print overhanging voxels as the meniscus was established and broken laterally. (c) The letters "E", "T", and "H" printed using this method (image taken at a 30°). The scale bar is the same for all three micrographs of the separate letters.

feedback mechanism that eliminates this issue. The operational principle is illustrated in Figure 1b. The nozzle approaches the biased substrate while the electrical current is constantly monitored (I) with a high gain current amplifier. The bias is chosen to a value more negative than the onset potential of the electroreduction (−0.29 V for copper, Supporting Information SI-2). When the nozzle is suspended in air, no electrical current is measured and the signal is determined by the electrical noise. As the tip of the nanopipette is brought close enough to the substrate, a liquid meniscus is formed that completes the electrical flow path and the electrodeposition process starts. The magnitude of the current rapidly increases and as soon as it exceeds the user-defined threshold (II) the pipette is retracted until the current value drops below the set point (III). If the feedback threshold is small enough, the meniscus breaks and the current stops flowing. Then, the pipette reapproaches the substrate (IV) and the process repeats (V) until the desired voxel height is printed, as monitored by the piezopositioner's sensor. In each cycle, the meniscus exists for only a few milliseconds (∼1000 times faster than in other approaches[24]), and the electroreduction results in a few nanometers-thick chemically pure metal layer (Supporting Information SI-3 and SI-4).

Figure 1c−e demonstrate the capabilities of this approach for submicroscale AM with a relatively large nozzle (diameter 253 nm). An array of pillars forming a 3D Gaussian peak (Figure 1c) was printed in a layer-by-layer approach comprising 656 voxels with 240 nm individual voxel heights. The surface of the pillars reveals single layers resulting from individual cycles of electrodeposition. Figure 1d,e demonstrates that this approach is also suitable for producing more intricate geometries that deviate from the simple straight vertical shapes and highlights the method's 3D capabilities. The layer-by-layer fabrication of four curved helix-like features further illustrates this, with the top view of the helices in Figure 1e showing the precision and print quality of the closely positioned features.

Control of the Printing Process. Interestingly, the feature size strongly depends on the electrodeposition parameters, namely, the printing voltage and the faradaic current (feedback threshold). These determine the quantity of metal deposited at each cycle of the process. Figure 2a,b reveals the effect of the printing potential (−0.55 to −0.35 V with a constant feedback threshold of −4 pA) on the feature size, printed with a 45 nm aperture nozzle. The diameters of the printed pillars extracted from the electron microscope image and as estimated from the data (Supporting Information SI-5) are summarized in Figure 2b. Estimating the feature size is convenient to track the printing process *in situ*, but there is a certain mismatch between the estimation and SEM measurement that originates from numerical errors in the current integration. The feature size increases linearly with the increase of the cathodic potential from 59 nm (±3 nm) at −0.35 V to 106 nm (±3 nm) at −0.55 V. Most likely, this result is caused by electrowetting that leads to a change in the solid−electrolyte contact angle at larger voltages, resulting in a larger meniscus footprint (Supporting Information SI-6). Also, the higher cathodic potential leads to increased current amplitudes and thus faster rate of deposition. Figure 2c shows the current trace of one of the printed columns in the array shown in Figure 2a. Despite the fixed threshold current of −4 pA, at larger cathodic voltages the currents tend to overshoot this value since the meniscus is not broken instantaneously. The zoomed-in view of single current peaks illustrates this effect in more detail. Although the threshold current for all the peaks is the same, at higher cathodic potentials the quick rise of the current significantly overshoots the set value of 4 pA, for example, −839 pA at −0.55 V, exceeding the threshold by >200-fold. The thickness of a single printed layer increases from 3 nm (±0.1 nm) at −0.35 V to 3.6 nm (±0.14 nm), 4.8 nm (±0.3 nm), 7.1 nm (±0.6 nm) and 10.7 nm (±1.1 nm) with each

https://doi.org/10.1021/acs.nanolett.1c02847
Nano Lett. 2021, 21, 9093−9101

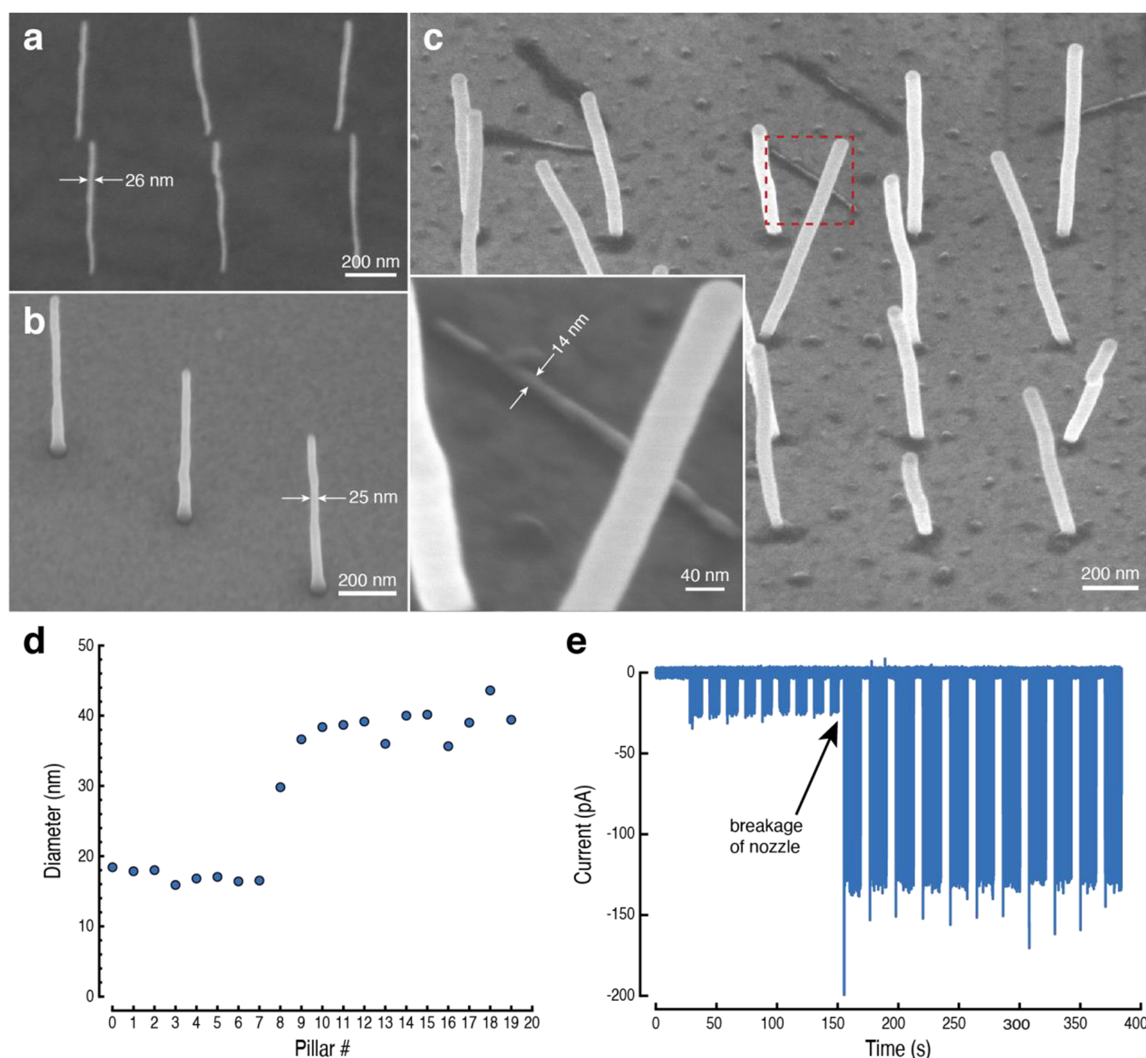

Figure 4. Approaching the resolution limit for electrochemical printing. SEM images of the smallest reproducible structures, printed with (a) 1.6 and (b) 2 nm aperture nozzles. (c) SEM image of the finest printed pillars observed in this work (irreproducible). After the 9th pillar, the nozzle seems to break probably due to clogging and the subsequent pillars were all fabricated with a thicker diameter. The inset in (c) shows a 14 nm (±2 nm) pillar (inset) lying on the substrate after having been printed upright (confirmed by growth data). (d) Estimated pillar diameters (from Faraday's law) and (e) the corresponding raw printing data illustrating the evolution of electrochemical currents during the printing. The arrow points at the time of nozzle breakage and thus increasing currents and larger diameters.

additional −0.05 V increment in voltage. This also has a drastic effect on the printing rate, which increases exponentially from 6.6 nm s^{-1} (±1.1 nm s^{-1}) at −0.35 V and reaching 69.7 nm s^{-1} (±7.4 nm s^{-1}) at −0.55 V (Supporting Information SI-7).

Similarly, the current threshold can be employed to control the feature size (Figure 2d). As shown, voxel diameters vary from 38 nm (±2 nm) at −5 pA to 71 nm (±3 nm) at −30 pA, thus depicting a similar trend as for varying voltage: larger quantity of injected charge results in a larger amount of electrodeposited material and thicker features. The current set point value, however, cannot strictly control the exact quantity of electrodeposited material, since on average the magnitude of the current at the peak overshoots this threshold by a few picoamperes higher (Figure 2e). Even at relatively low printing voltage as in this example (−0.35 V), the set point is exceeded by 1−5 pA. This overshoot is attributed to slow dynamics of the piezo actuators (typically, it takes 2−5 ms to break the meniscus after the set point is reached) as well as low data acquisition rates. Nevertheless, using appropriate set point values, stable and well-defined current maxima are established leading to uniformly grown structures.

Changing Voxel Size on-the-Fly. The possibility to alter feature dimensions by changing electrodeposition parameters allows one to vary the voxel size on-the-fly, that is, to 3D print objects consisting of features with variable diameter, which at the moment is offered only by a limited number of electrochemical AM techniques.[22] To demonstrate this capability, we repeatedly varied the electrodeposition voltage between −0.35 and −0.5 V within pillar structures constructed of 100 nm tall voxels fabricated in a layer-by-layer fashion with a 45 nm aperture nanopipette. Using the voltage to control the voxel dimensions is more practical as compared to the threshold current. Since eligible threshold current set points are dependent on the nozzle and meniscus geometry as well as the present current signal noise, thus more prone to miscalibration. Figure 2f demonstrates the result, where pillars in the front row contain voxels with iterative diameters (78 and 97 nm (both ±1.7 nm, about 20% change), and the pillars in the rear row are printed as a control at a constant voltage of

https://doi.org/10.1021/acs.nanolett.1c02847
Nano Lett. 2021, 21, 9093−9101

−0.5 V with a consistent diameter of 85 nm (±2.1 nm) throughout. Being able to change the diameter on-the-fly while printing without the need to change the print nozzle adds another degree of freedom to the manufacturing process and is a rather unexpected capability of meniscus-confined fabrication at this scale.

Nanoscale Tilted and Overhanging Structures. Layer-by-layer deposition is an almost absolute necessity for printing complex structures. To demonstrate the truly additive nature of the technique, we fabricated tilted structures and overhanging (up to 89°) parts. This can be achieved without the need for support structures. For tilted features, the printing principle is rather intuitive (inset of Figure 3a): each subsequent layer is shifted laterally by a small offset that determines the tilt angle. Larger offset distances result in higher tilt. Here, the lateral offsets were varied in a range from 0 (vertical pillar) to 14 nm to form tilted features at 0°, 11°, 22°, 31°, 39°, 45°, 50°, and 54° with 10 nm tall voxels (nozzle opening about 45 nm). Taking the vertical pillar as a reference, the resulting structures are tilted by 0°, 6°, 13°, 16°, 24°, 25°, 26°, and 37° (Figure 3a). These deviations (up to 62%) to the set tilt angles show the limitations of the method at the nanoscale. Drift of the piezo actuators as well as mechanical vibrations can lead to either missing of the last printed voxel or cause a mismatch between the subsequent layers.

Printing at angles >45° is challenging, as new layers grow on a small footprint of the previously printed structure. For these high tilt angles and for overhanging features (parallel to the substrate), the printing methodology needs to be adapted. For example, Hu and Yu[23] modified the pipette using focused ion beam milling to cut open one side of the nozzle, enabling lateral printing but only in the direction opposite to the cut. Here, another approach is introduced for fabrication of overhanging features. Instead of establishing and breaking the meniscus via the vertical translation, the nozzle movement occurs horizontally as shown schematically in Figure 3b. This way the meniscus is established and broken laterally, which causes the features to grow in this direction as well. Figure 3c illustrates the freestanding letters "ETH" printed in a layer-by-layer fashion with a mix of the two printing modes and a 45 nm diameter nozzle. Both the vertical and the horizontal features have a diameter of about 90 nm (±11 nm). One of the challenges in this printing mode, however, is creating a connection with other features, as evidenced by an incomplete horizontal bridge in the letter "H", although the gap is somewhat similar in dimensions to the voxel size itself. This issue arises due to a small nanoscale mismatch between the features to be connected. Despite that, printing overhangs from the same point, like in the letters "T" and "E", is trouble-free as evidenced by the well-defined features that form these structures.

Where Are the Limits of Electrochemical Printing? To answer this question, we employed nozzles with 1.6 and 2 nm apertures. These, to the best of our knowledge, are the smallest ever reported, not only for 3D printing but also for other applications, including electrochemical imaging[27] or single-molecule detection techniques. Figure 4a,b depicts the SEM images of the typical reproducibly printed features, where the diameters of the printed pillars are 25 nm (±2 nm). At this scale, even slight misalignment or vibrations could lead to buckles and bends in the printed pillars, and this effect is drastically more pronounced on thinner features than on larger objects. As illustrated in Figure 4c, in some rare cases printing of features as small as 14 nm (±2 nm) is also possible with the estimate from the printing data being around 16−18 nm (±1.4−2.7 nm, Figure 4d). This result, however, is irreproducible. In this example, after the ninth pillar the nozzle broke, most likely due to clogging, causing the following pillars to be larger as evidenced with higher printing currents (Figure 4e). As shown, the printing resolution approaches that of focused electron beam techniques and is at least an order of magnitude ahead of other similar electrochemical methods.

These results also indicate that there is a limit in printing resolution using the electrochemical meniscus-confined approach and features below 25−30 nm in size are difficult to fabricate even with ultrasmall nozzles. To determine where this limit is coming from, one has to consider the feedback that underlies the printing process. Here, it relies on the detection of the current flow during the meniscus presence on the substrate. Also, the faradaic current determines the amount of charge exchanged at the interface and therefore the amount of material plated. The smaller the meniscus, the taller a single deposited layer. In other words, with reducing the nozzle size the probability of the nozzle clogging increases, thus faster feedback is required.

To illustrate this quantitatively, one can calculate the limits of the nozzle size with the following assumptions (for our instrumentation): (i) currents as small as 3 pA can be reliably measured given the typical noise level; (ii) the shortest residence time of the meniscus on the substrate is about 3 ms; (iii) the printed feature size equals that of the nozzle aperture; and (iv) the meniscus height is roughly equal to the radius of the opening.[28] With these assumptions, one can estimate that when the nozzle diameter is about 9.4 nm, the height of the printed layer will be just below the meniscus height (Supporting Information SI-8). For smaller apertures, the clogging is inevitable: the thickness of the printed layer for our smallest nozzles with 1.6 nm opening is estimated to be 164.5 nm (>200 times than the meniscus height). The experimental results shown above are in good agreement with these calculations, indicating that the nozzles with single nanometer openings have a high propensity for clogging, resulting in their tips breaking off until the aperture size reaches dimensions where the risk of clogging greatly reduces. For larger apertures, this is not a problem anymore as the height of the deposited metal layer drops to about 0.6 nm for nozzles with 25 nm opening. Hence, as predicted by theory and confirmed by our experimental results, reproducible printing is only possible at scales from 25 nm and above.

Could this limitation be overcome, and electrochemical 3D printing limits be brought to a single-digit nanometer scale? In principle, this could be achieved by reducing the quantity of metal electrodeposited in a single printing cycle by about 3 orders of magnitude. This small amount of charge would approach the level of several attocoulombs (10^{-18} C), which is equivalent to only a few electrons transferred onto metal ions during a printing cycle. This miniscule amount of charge that should be equivalent to almost atom-by-atom fabrication, which is difficult to control at high acquisition rates (~kHz) required for reliable printing. Thus, electrochemical AM at this scale would require a drastically different approach, where the printing feedback will operate at fundamentally different (not based on faradaic current measurement) physical principles.

In summary, we demonstrated an approach to achieve nanoscale resolution in electrochemical 3D printing, that allows manufacturing of metal structures with dimensions

https://doi.org/10.1021/acs.nanolett.1c02847
Nano Lett. 2021, 21, 9093−9101

<100 nm, unattainable by other electrochemical methods. The printing process is broken down into repeated cycles of forming and ripping the liquid droplet between the nozzle and the substrate. This allows a controllable deposition of thin (few nm) layers of material and a synchronized fully automated retraction of the printing nozzle that eliminates the risk of nozzle clogging. This methodology is suitable for nozzles with a range of dimensions, from submicrometer down to only a few nanometers across, allowing full layer-by-layer printing capacity with on-the-fly voxel size control. We anticipate that further extension of this printing approach to other materials (after optimization of printing inks and electroplating conditions) will stimulate further development of 3D nanoprinting for a broad range of applications.

■ METHODS

Electrolyte Solution. The electrolyte solution for printing was prepared using 0.5 M of copper(II) sulfate pentahydrate ($CuSO_4·5H_2O$, Sigma-Aldrich, Switzerland) dissolved in 1 M sulfuric acid (H_2SO_4, Sigma-Aldrich, Switzerland). The concentration of 0.5 M was chosen in accordance with our preliminary experiments. It guarantees high print rates due to significant Cu^{2+} concentration and does not seem to cause issues with nozzle clogging. The final solution had a pH value of 0.4. Aqueous solutions were prepared using ultrapure deionized water with resistivity 18.2 MΩ cm at 25 °C (Milli-Q, Merck).

Nanopipettes. Nanopipettes were pulled using a commercial laser pipette puller (P2000, Sutter Instruments). The pipettes with 50, 2, or 1.48 nm nozzle openings were pulled from quartz capillaries with a filament and an outer diameter (OD) of 1 mm and an inner diameter (ID) of 0.5 mm (QF100-50-10, Friedrich & Dimmock). The pipettes with about 250 nm nozzle opening were pulled from borosilicate glass capillaries with a filament with 1.2 mm OD and 0.69 mm ID (Harvard Apparatus). The pulling parameters are listed in Supporting Information Table S1.

Electron Microscopy. Electron microscope images of nanopipettes were acquired with a transmission electron microscope (JEM-1400, JEOL) at 200 kV accelerating voltage. Printed metal structures were characterized by a scanning electron microscope (Magellan 400, FEI Company). A Helios 5 UX DualBeam FIB-SEM (Thermo Fisher Scientific, U.S.A.) was used to expose and image printed features' cross sections.

Substrate. All structures fabricated within this work were printed either on microscopy glass slides (Menzel) or silicon wafers that were on one side sputter coated with a 25 nm gold film on top of a sputter coated 3 nm Titanium film. No treatment or cleaning was performed prior to printing on the substrate. The substrates were glued with UV curable glue (3311, Loctite) onto aluminum SEM pin stubs (12.7 mm, Zeiss) used for fixation while printing and for later SEM analysis. Silver paint (EM-Tec AG15, Microtonano) was used to establish an electrical connection between the stub and the substrates gold surface.

Statistics. Statistical data is reported as a mean value ($N \geq 3$) with a 95% confidence interval where appropriate.

Nanoprinting Setup. Using a custom-made pipette holder, the electrolyte-filled nanopipettes were mounted above the substrate. A silver wire (0.125 mm, GoodFellow), employed as a quasi-reference counter electrode, was immersed into the electrolyte and connected to a voltage source. Coarse manual positioning of the pipette was performed with a micropositioner (MicroStage, MadCityLabs) for lateral movement of the stage (*XY*-axis), a micropositioning device (MMP1, MadCityLabs) to move the pipette vertical to the substrate (*Z*-axis) and an optical microscope camera (AM7915MZTL - EDGE, Dino Lite) for coarse optical control of the distance. To automatically approach the substrate, prior to printing the pipette was moved vertically by a piezo positioner (Nano-MET10, MadCityLabs) at a speed of 1 μm s^{-1} (0.15 nm s^{-1} for 1 nm aperture nozzles). The approach rate was chosen to provide a safe vertical nozzle translation without the risk of crashing into the substrate before the meniscus can be detected, given the rate of data acquisition (1953 Hz, sampling every 512 μs) and vertical piezo position update rate (1 nm ms^{-1} or 0.15 nm ms^{-1} for single nanometer nozzles). During the approach, the current was recorded continuously using a current amplifier (DLPCA-200, Femto). If a preset threshold current of −3 to −20 pA was exceeded, marking the formation of a liquid meniscus between nozzle tip and substrate, the pipette was immediately retracted. If no such event was detected within the 10 μm range of the piezo positioner, the positioner was retracted for 10 μm and the pipette was moved to the substrate using the micropositioner by 10 μm. The actual printing was performed using a subnanometer precision *XY* piezo stage (Nano-PDQ250, MadCityLabs). The approach rate used while printing was 1 μm s^{-1} (0.15 nm s^{-1} for 1 nm aperture nozzles), while the retract speed to break the meniscus was 30−50 times faster (30−50 μm s^{-1}). Throughout the whole printing process, the pipette position was monitored using the sensing capabilities of the piezo positioners. Acquired *z*-coordinates at each landing (when meniscus is detected) enabled one to precisely monitor the height of each deposited layer with subnanometer resolution as well as to track the overall progress in fabrication of the whole structure. This data was later used to provide the height information for estimation of the diameter using Faraday's law (see Supporting Information SI-5). In combination with the *X*- and *Y*-coordinates at meniscus formation, an observation of the printed structure during fabrication is possible. The control of the setup and acquisition of the raw data was performed using a PC equipped with an FPGA card (PCIe-7846, National Instruments) and a custom-made LabVIEW program based on the WEC-SPM software package (provided by Prof. Unwin, University of Warwick). The printing environment was not controlled deliberately but the temperature was measured to be stable at around 23 °C whereas the relative humidity deviated between 30% and 60%. Preliminary experiments at different relative humidity levels had no influence on the printing results, hence it was not controlled in the current study.

The meniscus formation occurs by a mechanical contact between the substrate and a sessile droplet at the hydrophilic tip of the glass pipette. No additional pressure control is needed to initiate the formation of this droplet or the liquid meniscus, allowing printing without additional microfluidic instrumentation.

To reduce the magnitude of electromagnetic noise, the whole setup was enclosed in a custom-made faraday cage. To reduce acoustic noise and mechanical vibrations, the stage was placed on a benchtop vibration isolation platform (BM-8, Minus K Technology) and the faraday cage lined with acoustic foam.

https://doi.org/10.1021/acs.nanolett.1c02847
Nano Lett. 2021, 21, 9093−9101

ASSOCIATED CONTENT

Supporting Information

The Supporting Information is available free of charge at https://pubs.acs.org/doi/10.1021/acs.nanolett.1c02847.

Characterization of pulled nanopipette nozzles, cyclic voltammetry, EDS analysis, deposited layers characterization, estimation of voxel diameters using Faraday's law, meniscus electrowetting, printing rates, and calculation of the nozzle clogging limit (PDF)

AUTHOR INFORMATION

Corresponding Author

Dmitry Momotenko − *Laboratory of Biosensors and Bioelectronics, Institute for Biomedical Engineering, ETH Zurich, Zurich CH-8092, Switzerland; Department of Chemistry, Carl von Ossietzky University of Oldenburg, Oldenburg D-26129, Germany;* orcid.org/0000-0003-0302-4916; Email: dmitry.momotenko@uol.de

Authors

Julian Hengsteler − *Laboratory of Biosensors and Bioelectronics, Institute for Biomedical Engineering, ETH Zurich, Zurich CH-8092, Switzerland*

Barnik Mandal − *Laboratory of Biosensors and Bioelectronics, Institute for Biomedical Engineering, ETH Zurich, Zurich CH-8092, Switzerland*

Cathelijn van Nisselroy − *Laboratory of Biosensors and Bioelectronics, Institute for Biomedical Engineering, ETH Zurich, Zurich CH-8092, Switzerland*

Genevieve P. S. Lau − *School of Physical and Mathematical Sciences, Division of Chemistry and Biological Chemistry, Nanyang Technological University, 637371, Singapore*

Tilman Schlotter − *Laboratory of Biosensors and Bioelectronics, Institute for Biomedical Engineering, ETH Zurich, Zurich CH-8092, Switzerland*

Tomaso Zambelli − *Laboratory of Biosensors and Bioelectronics, Institute for Biomedical Engineering, ETH Zurich, Zurich CH-8092, Switzerland*

Complete contact information is available at: https://pubs.acs.org/10.1021/acs.nanolett.1c02847

Notes

The authors declare no competing financial interest.

ACKNOWLEDGMENTS

This project has received funding from the European Research Council (ERC) under the European Union's Horizon 2020 research and innovation programme (Grant Agreement 948238). The authors also acknowledge funding from ETH Zürich (ETH Grant ETH-42-19.1, T.Z. and D.M.) and the Swiss National Science Foundation, including Ambizione (PZ00P2_174217, D.M.) and SPARK (CRSK-2_190211, D.M.) grants. G.L. is grateful for support from Nanyang Technological University (Presidential Postdoctroal Fellowship, Grant 04INS000542C230). The authors acknowledge Prof. Unwin, University of Warwick, for providing the WEC-SPM software package used for pipette manipulation and data-acquisition. For the support and assistance with electron microscopy imaging we acknowledge the Scientific Center for Optical and Electron Microscopy (ScopeM, ETH Zurich) and in particular Dr. Joakim Reuteler. We also acknowledge the technical assistance of Stephen Wheeler (ETH Zurich).

REFERENCES

(1) Stewart, M. E.; Anderton, C. R.; Thompson, L. B.; Maria, J.; Gray, S. K.; Rogers, J. A.; Nuzzo, R. G. Nanostructured Plasmonic Sensors. *Chem. Rev.* **2008**, *108* (2), 494−521.

(2) Anandan, V.; Yang, X.; Kim, E.; Rao, Y. L.; Zhang, G. Role of Reaction Kinetics and Mass Transport in Glucose Sensing with Nanopillar Array Electrodes. *J. Biol. Eng.* **2007**, *1*, 5.

(3) Dong, M.; Wang, X.; Chen, X.-Z.; Mushtaq, F.; Deng, S.; Zhu, C.; Torlakcik, H.; Terzopoulou, A.; Qin, X.-H.; Xiao, X.; Puigmartí-Luis, J.; Choi, H.; Pêgo, A. P.; Shen, Q.-D.; Nelson, B. J.; Pané, S. 3D-Printed Soft Magnetoelectric Microswimmers for Delivery and Differentiation of Neuron-Like Cells. *Adv. Funct. Mater.* **2020**, *30* (17), 1910323.

(4) Sánchez, S.; Soler, L.; Katuri, J. Chemically Powered Micro- and Nanomotors. *Angew. Chem., Int. Ed.* **2015**, *54* (5), 1414−1444.

(5) Park, J.; Kim, J.; Pané, S.; Nelson, B. J.; Choi, H. Acoustically Mediated Controlled Drug Release and Targeted Therapy with Degradable 3D Porous Magnetic Microrobots. *Adv. Healthcare Mater.* **2021**, *10*, 2001096.

(6) Sun, K.; Wei, T.-S.; Ahn, B. Y.; Seo, J. Y.; Dillon, S. J.; Lewis, J. A. 3D Printing of Interdigitated Li-Ion Microbattery Architectures. *Adv. Mater.* **2013**, *25* (33), 4539−4543.

(7) Kohlmeyer, R. R.; Blake, A. J.; Hardin, J. O.; Carmona, E. A.; Carpena-Núñez, J.; Maruyama, B.; Berrigan, J. D.; Huang, H.; Durstock, M. F. Composite Batteries: A Simple yet Universal Approach to 3D Printable Lithium-Ion Battery Electrodes. *J. Mater. Chem. A* **2016**, *4* (43), 16856−16864.

(8) Egorov, V.; Gulzar, U.; Zhang, Y.; Breen, S.; O'Dwyer, C. Evolution of 3D Printing Methods and Materials for Electrochemical Energy Storage. *Adv. Mater.* **2020**, *32* (29), 2000556.

(9) Haske, W.; Chen, V. W.; Hales, J. M.; Dong, W.; Barlow, S.; Marder, S. R.; Perry, J. W. 65 Nm Feature Sizes Using Visible Wavelength 3-D Multiphoton Lithography. *Opt. Express* **2007**, *15* (6), 3426−3436.

(10) Fischer, J.; Wegener, M. Three-Dimensional Direct Laser Writing Inspired by Stimulated-Emission-Depletion Microscopy [Invited]. *Opt. Mater. Express* **2011**, *1* (4), 614.

(11) Utke, I.; Hoffmann, P.; Melngailis, J. Gas-Assisted Focused Electron Beam and Ion Beam Processing and Fabrication. *J. Vac. Sci. Technol. B Microelectron. Nanometer Struct.* **2008**, *26* (4), 1197.

(12) Winkler, R.; Fowlkes, J. D.; Rack, P. D.; Plank, H. 3D Nanoprinting via Focused Electron Beams. *J. Appl. Phys.* **2019**, *125* (21), 210901.

(13) Mitsuishi, K.; Shimojo, M.; Han, M.; Furuya, K. Electron-Beam-Induced Deposition Using a Subnanometer-Sized Probe of High-Energy Electrons. *Appl. Phys. Lett.* **2003**, *83* (10), 2064−2066.

(14) Shimojo, M.; Mitsuishi, K.; Tanaka, M.; Han, M.; Furuya, K. Application of Transmission Electron Microscopes to Nanometre-Sized Fabrication by Means of Electron Beam-Induced Deposition. *J. Microsc.* **2004**, *214* (1), 76−79.

(15) Luisier, A.; Utke, I.; Bret, T.; Cicoira, F.; Hauert, R.; Rhee, S.-W.; Doppelt, P.; Hoffmann, P. Comparative Study of Cu-Precursors for 3D Focused Electron Beam Induced Deposition. *J. Electrochem. Soc.* **2004**, *151* (9), C590.

(16) Hirt, L.; Grüter, R. R.; Berthelot, T.; Cornut, R.; Vörös, J.; Zambelli, T. Local Surface Modification via Confined Electrochemical Deposition with FluidFM. *RSC Adv.* **2015**, *5* (103), 84517−84522.

(17) Daryadel, S.; Behroozfar, A.; Morsali, S. R.; Moreno, S.; Baniasadi, M.; Bykova, J.; Bernal, R. A.; Minary-Jolandan, M. Localized Pulsed Electrodeposition Process for Three-Dimensional Printing of Nanotwinned Metallic Nanostructures. *Nano Lett.* **2018**, *18* (1), 208−214.

(18) Wang, C.; Hossain Bhuiyan, M. E.; Moreno, S.; Minary-Jolandan, M. Direct-Write Printing Copper−Nickel (Cu/Ni) Alloy with Controlled Composition from a Single Electrolyte Using Co-Electrodeposition. *ACS Appl. Mater. Interfaces* **2020**, *12* (16), 18683−18691.

(19) Hirt, L.; Ihle, S.; Pan, Z.; Dorwling-Carter, L.; Reiser, A.; Wheeler, J. M.; Spolenak, R.; Vörös, J.; Zambelli, T. Template-Free

3D Microprinting of Metals Using a Force-Controlled Nanopipette for Layer-by-Layer Electrodeposition. *Adv. Mater.* **2016**, *28* (12), 2311−2315.

(20) Momotenko, D.; Page, A.; Adobes-Vidal, M.; Unwin, P. R. Write−Read 3D Patterning with a Dual-Channel Nanopipette. *ACS Nano* **2016**, *10* (9), 8871−8878.

(21) Ercolano, G.; van Nisselroy, C.; Merle, T.; Vörös, J.; Momotenko, D.; Koelmans, W. W.; Zambelli, T. Additive Manufacturing of Sub-Micron to Sub-Mm Metal Structures with Hollow AFM Cantilevers. *Micromachines* **2020**, *11* (1), 6.

(22) Ercolano, G.; Zambelli, T.; van Nisselroy, C.; Momotenko, D.; Vörös, J.; Merle, T.; Koelmans, W. W. Multiscale Additive Manufacturing of Metal Microstructures. *Adv. Eng. Mater.* **2020**, *22* (2), 1900961.

(23) Hu, J.; Yu, M.-F. Meniscus-Confined Three-Dimensional Electrodeposition for Direct Writing of Wire Bonds. *Science* **2010**, *329* (5989), 313−316.

(24) Lin, Y.-P.; Zhang, Y.; Yu, M.-F. Parallel Process 3D Metal Microprinting. *Adv. Mater. Technol.* **2019**, *4* (1), 1800393.

(25) Lei, Y.; Zhang, X.; Xu, D.; Yu, M.; Yi, Z.; Li, Z.; Sun, A.; Xu, G.; Cui, P.; Guo, J. Dynamic "Scanning-Mode" Meniscus Confined Electrodepositing and Micropatterning of Individually Addressable Ultraconductive Copper Line Arrays. *J. Phys. Chem. Lett.* **2018**, *9* (9), 2380−2387.

(26) Eliyahu, D.; Gileadi, E.; Galun, E.; Eliaz, N. Atomic Force Microscope-Based Meniscus-Confined Three-Dimensional Electrodeposition. *Adv. Mater. Technol.* **2020**, *5* (2), 1900827.

(27) Zhu, C.; Huang, K.; Siepser, N. P.; Baker, L. A. Scanning Ion Conductance Microscopy. *Chem. Rev.* **2020**, DOI: 10.1021/acs.chemrev.0c00962.

(28) Aaronson, B. D. B.; Güell, A. G.; McKelvey, K.; Momotenko, D.; Unwin, P. R. Scanning Electrochemical Cell Microscopy, Mapping, Measuring, and Modifying Surfaces and Interfaces at the Nanoscale. In *Nanoelectrochemistry*, 1st ed.; CRC Press, 2015; pp 655−687.